Journal of Computational Physics **165,** 522–541 (2000)
doi:10.1006/jcph.2000.6631, available online at http://www.idealibrary.com on IDEAL®

Prefactored Small-Stencil Compact Schemes

R. Hixon

Institute for Computational Mechanics in Propulsion, NASA Glenn Research Center, Cleveland, Ohio 44135
E-mail: fshixon@apu.grc.nasa.gov

Received September 7, 1999; revised August 21, 2000

A new type of prefactored compact schemes is presented that obtains high-order accuracy while using a very small stencil size. These schemes require fewer boundary stencils and offer simpler boundary condition implementation than the existing compact schemes. Results are shown for linear and nonlinear 1-D benchmark problems and a 2-D linear benchmark problem. Boundary stencils for both exterior and interior multiblock boundaries are given, and boundary condition specification is described and demonstrated.

Key Words: compact differencing; high-order finite differences; computational aeroacoustics.

1. INTRODUCTION

The field of computational aeroacoustics is focused on obtaining long-term, time-accurate numerical solutions to unsteady flow and acoustic problems. In order to accomplish this, a high-accuracy time-marching scheme is combined with high-resolution spatial derivatives. There are two main classes of high-accuracy finite-difference schemes: explicit schemes and compact schemes (e.g., Refs. [1–12]). Explicit schemes use large computational stencils for accuracy, while compact schemes use smaller stencils by implicitly solving for the spatial derivatives at each grid point. While compact schemes are more accurate than the equivalent explicit schemes, they have two disadvantages: first, a linear system must be solved to obtain the spatial derivative at a point; second, the boundary stencil has a large effect on the stability and accuracy of the scheme.

Recently, a new class of high-accuracy compact MacCormack-type schemes for computational aeroacoustics have been derived [12]. These schemes use a prefactorization method to reduce a nondissipative central-difference stencil to two lower-order biased stencils which have easily solved reduced matrices. However, there are drawbacks to high-accuracy MacCormack-type schemes. If the inherent damping in the biased stencil is too large, it can damp out waves which the original central-difference stencil could propagate accurately. If the inherent damping in the biased stencil is too small, nonlinear waves may

0021-9991/00 $35.00

generate unresolved high-frequency waves that will destroy the solution accuracy [11]. To avoid these problems while keeping the advantages of the easily solved prefactored matrices, new types of nondissipative prefactored high-order compact schemes are derived which uses three-point stencils and returns up to eighth-order accuracy.

2. DESCRIPTION OF COMPACT SCHEMES

A general compact derivative of a function f may be written as

$$[B]\{D\} = \frac{1}{\Delta x}[C]\{f\}, \tag{1}$$

where D is the spatial derivative of the function f, and $[B]$ is an easily solved linear system. Expanding this equation for a general pentadiagonal system at point i gives

$$\begin{aligned}\gamma(D_{i+2} + D_{i-2}) + \beta(D_{i+1} + D_{i-1}) + (1 - \gamma - \beta)D_i \\ = \frac{1}{\Delta x}[\varphi(f_{i+2} - f_{i-2}) + \eta(f_{i+1} - f_{i-1})].\end{aligned} \tag{2}$$

For fourth-order accuracy,

$$\begin{aligned}\gamma &= 0 \\ \beta &= \frac{1}{6} \\ \varphi &= 0 \\ \eta &= \frac{1}{2}.\end{aligned} \tag{3}$$

For sixth-order accuracy,

$$\begin{aligned}\gamma &= 0 \\ \beta &= \frac{1}{5} \\ \varphi &= \frac{1}{60} \\ \eta &= \frac{7}{15}.\end{aligned} \tag{4}$$

For eighth-order accuracy,

$$\begin{aligned}\gamma &= \frac{1}{70} \\ \beta &= \frac{8}{35} \\ \varphi &= \frac{5}{84} \\ \eta &= \frac{8}{21}.\end{aligned} \tag{5}$$

There are several interesting features of these compact schemes. The first is that the linear systems for the fourth- and sixth-order compact schemes contain tridiagonal matrices, while

the eighth-order scheme contains a pentadiagonal matrix. The second point is that the fourth-order scheme requires one boundary stencil, while the sixth- and eighth-order schemes each require two boundary stencils due to their larger computational stencils.

3. MATHEMATICAL FORMULATION OF PREFACTORED COMPACT SCHEMES

Following the development given in Ref. [12], we define forward and backward derivative operators,

$$D_i = \frac{1}{2}\left(D_i^F + D_i^B\right), \tag{6}$$

where

$$\begin{aligned} [B^F]\{D^F\} &= \frac{1}{\Delta x}[C^F]\{f\} \\ [B^B]\{D^B\} &= \frac{1}{\Delta x}[C^B]\{f\}. \end{aligned} \tag{7}$$

We introduce the restriction

$$\begin{aligned} [B^F] &= [B^B]^T \\ [C^F] &= -[C^B]^T, \end{aligned} \tag{8}$$

which allows Eq. (7) to be rewritten as

$$\begin{aligned} aD_{i+1}^F + (1-a-c)D_i^F + cD_{i-1}^F &= \frac{1}{\Delta x}[bf_{i+1} - (2b-1)f_i - (1-b)f_{i-1}] \\ cD_{i+1}^B + (1-a-c)D_i^B + aD_{i-1}^B &= \frac{1}{\Delta x}[(1-b)f_{i+1} + (2b-1)f_i - bf_{i-1}]. \end{aligned} \tag{9}$$

Substituting into Eq. (6), we find

$$[B^B][B^B]^T\{D\} = \frac{1}{2\Delta x}([B^B]^T[C^B] - [B^B][C^B]^T)\{f\} \tag{10}$$

or

$$\begin{aligned} &(ac)(D_{i+2} + D_{i-2}) + (a+c)(1-a-c)(D_{i+1} + D_{i-1}) + (a^2 + c^2 + (1-a-c)^2)D_i \\ &\quad = \frac{1}{\Delta x}\left[\begin{array}{l} \frac{1}{2}(a + b(c-a))(f_{i+2} - f_{i-2}) \\ \quad + \left(\frac{1}{2} - a - b(c-a)\right)(f_{i+1} - f_{i-1}) \end{array}\right]. \end{aligned} \tag{11}$$

As stated in Ref. [12], obtaining Eq. (10) requires that

$$[B^B][B^B]^T = [B^B]^T[B^B], \tag{12}$$

which is true in the interior of constant-coefficient tridiagonal matrices.

By comparing Eq. (11) to Eq. (2), a new type of small-stencil compact schemes can be derived where

$$
\begin{aligned}
a &= \frac{1}{4} - \frac{1}{2}\sqrt{\frac{1}{4} - \beta} - \frac{1}{2}\sqrt{\frac{1}{2} - \beta - 4\gamma - \frac{1 + 8\gamma - 4(\beta + 2\gamma)}{4\sqrt{\frac{1}{4} - \beta}}} \\
b &= a^2 - \frac{a(a - 2\varphi)}{\gamma} \\
c &= \frac{\gamma}{a}.
\end{aligned}
\tag{13}
$$

For fourth-order accuracy, from Ref. [12]:

$$
\begin{aligned}
a &= \frac{1}{2} - \frac{1}{2\sqrt{3}} \\
b &= 1 \\
c &= 0.
\end{aligned}
\tag{14}
$$

Notice that the operators are fully one-sided on a two-point stencil for fourth-order accuracy. Also, since $c = 0$, the matrix is reduced from one tridiagonal matrix to two independent bidiagonal matrices which can be solved by sweeping.

For sixth-order accuracy:

$$
\begin{aligned}
a &= \frac{1}{2} - \frac{1}{2\sqrt{5}} \\
b &= 1 - \frac{1}{30a} \\
c &= 0.
\end{aligned}
\tag{15}
$$

This time, the stencil is reduced from five points to three points, with the tridiagonal matrix replaced by two independent bidiagonal matrices. Figure 1 compares the performance of the sixth-order scheme with those of an explicit sixth-order scheme and the widely used 7-point Dispersion Relation Preserving explicit scheme for the spatial derivative of a simple-harmonic waveform with a given number of grid points per wavelength. Notice that the sixth-order compact scheme has much less error than the explicit schemes for a given number of grid points per wavelength.

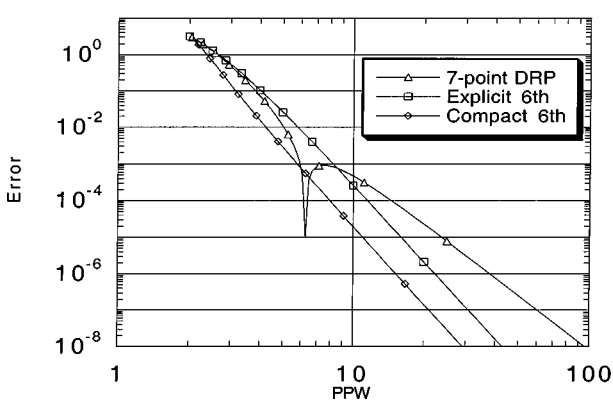

FIG. 1. Error comparison of compact and explicit schemes.

This is not the only possible prefactorization for the sixth-order scheme. Another prefactorization exists where the explicit stencil is fully one-sided rather than centered. However, with this prefactorization, the final stencil still uses five points.

For eighth-order accuracy,

$$\begin{aligned} a &= \frac{1}{4} - \frac{1}{4}\sqrt{\frac{3}{35}} - \frac{1}{2}\sqrt{\frac{3}{14} - \frac{1}{2}\sqrt{\frac{3}{35}}} \\ b &= \frac{70}{69}\left(a^2 - \frac{5a}{42}\right) \\ c &= \frac{1}{70a}. \end{aligned} \tag{16}$$

The eighth-order stencil has been reduced from five points to three points, with the single pentadiagonal matrix being replaced by two independent tridiagonal matrices. Again, there are other possible prefactorizations which result in larger stencil sizes.

The Taylor series expansion of the forward and backward operators for the fourth-order scheme can be written as

$$\begin{aligned} D^F &= \frac{df}{dx} + \frac{\sqrt{3}}{6}\Delta x\frac{d^2f}{dx^2} - \frac{\sqrt{3}}{72}(\Delta x)^3\frac{d^4f}{dx^4} + \vartheta(\Delta x)^4 \\ D^B &= \frac{df}{dx} - \frac{\sqrt{3}}{6}\Delta x\frac{d^2f}{dx^2} + \frac{\sqrt{3}}{72}(\Delta x)^3\frac{d^4f}{dx^4} + \vartheta(\Delta x)^4. \end{aligned} \tag{17}$$

Note that the even derivatives are equal and opposite between the two operators, and cancel when the two operators are added. The odd derivatives are equal and remain when the two operators are added. It should be noted that, while these operators could be used in a MacCormack-type scheme, the inherent dissipation from the leading error terms would damp the high-frequency waves that the improved accuracy would otherwise capture.

From this point on, all results are for the sixth-order compact scheme, but all concepts are applicable to the other schemes.

4. COMPARISION OF PREFACTORED AND STANDARD SIXTH-ORDER COMPACT SCHEME

The Thomas algorithm for a scalar, constant coefficient tridiagonal matrix is written as follows:

For $j = 1$,

$$\begin{aligned} \xi_1 &= \frac{1}{F} \\ D_1 &= R_1\xi_1. \end{aligned} \tag{18}$$

Do $j = 2$, j max,

$$\begin{aligned} \lambda_j &= G\xi_{j-1} \\ \xi_j &= \frac{1}{F - E\lambda_j} \\ D_j &= (R_j - E D_{j-1})\xi_j. \end{aligned} \tag{19}$$

Do $j = j\max -1, 1, -1$,

$$D_j = D_j - \lambda_{j+1} D_{j+1}. \tag{20}$$

For the sixth-order compact scheme,

$$\begin{aligned} E &= \frac{1}{5} \\ F &= \frac{3}{5} \\ G &= \frac{1}{5} \\ R_j &= \left[\frac{1}{60\Delta x}(f_{j+2} - f_{j-2}) + \frac{7}{15\Delta x}(f_{j+1} - f_{j-1})\right]. \end{aligned} \tag{21}$$

To obtain the spatial derivative using this scheme, first the right hand side of the equation R_j must be computed. This takes two multiplications and three additions per point. Next, the forward and backward sweeps are performed (Eqs. (19) and (20)). This requires four multiplications, one division, and two additions at each point for the first sweep and one multiplication and one addition at each point for the backsubstitution sweep. This gives a total of seven multiplications, one division, and six additions per point for the entire Thomas algorithm.

To save work, λ and ξ can be calculated once, saved, and reused each time. This reduces the forward sweep to two multiplications and one addition, for a total of five multiplications and five additions per point for each derivative. By premultiplying the equation to set $E = 1$, one multiplication per point can be removed, giving four multiplications and five additions per point for the most efficient Thomas algorithm.

The prefactored form of the sixth-order compact scheme can be written as

$$\begin{aligned} \frac{1}{2}D_j^F &= \left[\frac{b}{2\Delta x(1-a)}(f_{j+1} - f_j) + \frac{1-b}{2\Delta x(1-a)}(f_j - f_{j-1})\right] - \frac{1}{2}\left(\frac{a}{1-a}\right)D_{j+1}^F \\ \frac{1}{2}D_j^B &= \left[\frac{b}{2\Delta x(1-a)}(f_j - f_{j-1}) + \frac{1-b}{2\Delta x(1-a)}(f_{j+1} - f_j)\right] - \frac{1}{2}\left(\frac{a}{1-a}\right)D_{j-1}^B. \end{aligned} \tag{22}$$

Using the prefactored form of the sixth-order compact scheme, the right-hand-side of the equations also requires three additions and two multiplications to obtain. Each sweep requires one addition and one multiplication per point for a total of two additions and two multiplications per point. Finally, the results are added together, giving a total of four multiplications and six additions per point, one addition per point more than the most optimized Thomas algorithm. Since additions are much less expensive than multiplications, the advantages of the prefactorization offset the slight increase in computational cost.

5. BOUNDARY SPECIFICATION FOR PREFACTORED COMPACT SCHEME

Many common boundary conditions require the user to correct the normal derivative at the boundary by taking into account information from the normal and tangential derivatives

at the boundary. Some examples are Thompson's characteristic boundary condition [13, 14] and Tam and Dong's wall boundary condition [15]. In this section, we will investigate how this is accomplished in the standard and prefactored compact schemes.

For the Thomas algorithm, if there is an error in the boundary derivative, it will appear in the first or last point in the right-hand-side vector. To correct the solution in the interior, either the entire matrix will have to be solved again, or the corrected result will have to be checked against the original result until the error is tolerable. If the corrected boundary is at the beginning of the backward sweep, only the backward sweep will have to be corrected. If the corrected boundary is at the start of the forward sweep, both sweeps will have to be corrected. To avoid having to completely solve the matrix, the intermediate result from the forward sweep will have to be stored until the boundary condition is complete.

For the prefactored scheme, only the correction to the boundary derivative will have to be propagated into the domain. To illustrate, let us assume we have an error ε_0 from the boundary derivative at the beginning of the backward sweep, defining ε_0 as

$$\varepsilon_0 = D^B_{\text{corrected}} - D^B_{\text{computed}}, \tag{23}$$

where the subscript "corrected" refers to the spatial derivative that has been corrected by the boundary condition and the subscript "computed" refers to the derivative obtained by the code.

Substituting into Eq. (9), we find that

$$\left(D^B_i\right)_{\text{corrected}} = \left(D^B_i\right)_{\text{computed}} + \left(-\frac{a}{1-a}\right)^i \varepsilon_0 \tag{24}$$

or

$$\varepsilon_i = \left(-\frac{a}{1-a}\right)^i \varepsilon_0. \tag{25}$$

Note that it is easily determined how to correct the derivative error using the prefactored scheme as compared to the Thomas algorithm. This is because the Thomas algorithm is an LU scheme, while the prefactored scheme is an L + U scheme.

6. BOUNDARY STENCILS FOR THE PREFACTORED SIXTH-ORDER COMPACT SCHEME

6.1. *Effect of Boundary Stencil on Interior Scheme*

The numerical performance of the boundary stencil for a compact scheme has a much larger effect on the stability and accuracy of the scheme than the boundary stencil for the equivalent explicit scheme (e.g., Refs. [15–18]). The reason for this is that the error from the boundary stencil derivative can propagate many points into the computational domain.

Taking the sixth-order scheme as an example, let us assume we have an error ε_0 from the boundary at the beginning of the backward sweep, defining ε_0 as

$$\varepsilon_0 = D^B_{\text{interior}} - D^B_{\text{boundary}}, \tag{26}$$

where the subscript "interior" refers to the spatial derivative that the interior scheme would have obtained and the subscript "boundary" refers to the derivative obtained by the boundary

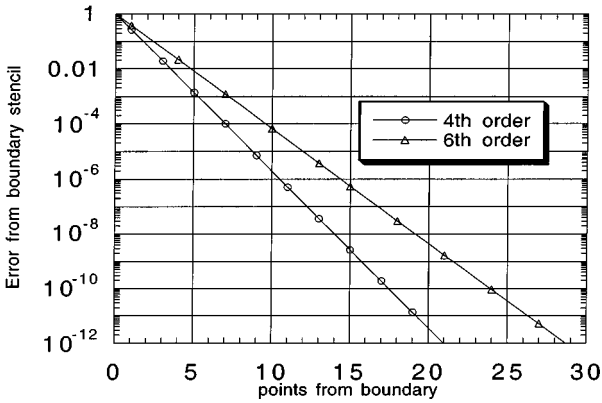

FIG. 2. Effect of boundary stencil error on interior points.

stencil. Notice that we are defining the error with respect to the spatial derivative that the interior scheme would have obtained rather than the exact analytical derivative.

Substituting into Eq. (9), we find that

$$\left(D_i^B\right)_{\text{interior}} = \left(D_i^B\right)_{\text{boundary}} + \left(-\frac{a}{1-a}\right)^i \varepsilon_0 \tag{27}$$

or

$$\varepsilon_i = \left(-\frac{a}{1-a}\right)^i \varepsilon_0 \tag{28}$$

One point of interest is that the error due to the boundary stencil used at the start of the forward or backward sweep has a much greater effect on the solution than that of the boundary stencil used at the end of the sweep. Due to the tridiagonal matrices in the eighth-order scheme, both stencils have an effect on the interior error.

Equations (27) and (28) are valid for the fourth- and sixth-order compact schemes, but not for the eighth-order scheme, due to the tridiagonal matrix. Figure 2 illustrates the effect of boundary stencil error for the fourth- and sixth-order compact schemes. Notice that the sixth-order scheme has much more dependence on the boundary stencil error than the fourth-order scheme has. This is due to the larger effective stencil used by the sixth-order scheme.

6.2. *One-Sided Boundary Stencils*

For use at the outer boundary and wall points, explicit sixth-order, one-sided derivative stencils were derived for the sixth-order compact scheme. To accomplish this, the Taylor series for the forward and backward interior derivatives was matched to the sixth order. The resulting boundary stencils are

$$\begin{aligned} D_1^B &= \sum_{j=1}^{7} s_j f_j \\ D_{j\max}^B &= \sum_{j=j\max-6}^{j\max} e_j f_j, \end{aligned} \tag{29}$$

where

$$\begin{aligned} s_1 &= -2.748875 \\ s_2 &= 6.9122653 \\ s_3 &= -8.5709877 \\ s_4 &= 7.29077104 \\ s_5 &= -3.93792558 \\ s_6 &= 1.22040498 \\ s_7 &= -0.165322497 \end{aligned} \tag{30}$$

and

$$\begin{aligned} e_{j\max} &= 2.151125 \\ e_{j\max-1} &= -5.087735 \\ e_{j\max-2} &= 6.429012 \\ e_{j\max-3} &= -6.042892 \\ e_{j\max-4} &= 3.562074 \\ e_{j\max-5} &= -1.179594 \\ e_{j\max-6} &= 0.168011. \end{aligned} \tag{31}$$

For the forward sweep,

$$\begin{aligned} D_1^F &= \sum_{j=1}^{7} -e_{j\max+1-j}\, f_j \\ D_{j\max}^F &= \sum_{j=j\max-6}^{j\max} -s_{j\max+1-j}\, f_j \end{aligned} \tag{32}$$

To investigate the stability of the prefactored sixth-order compact scheme and compare it with the standard sixth-order scheme, a spectral eigenvalue analysis was done using the linear equation

$$D^{\text{diss}} = \frac{A}{2}(D^F - D^B)u_t = -u_x. \tag{33}$$

The computational domain consisted of 81 equally spaced points. Since the standard sixth-order compact scheme requires two boundary stencils, biased explicit sixth-order stencils were used for these points. Thus, the stencil at the boundary point for the standard scheme is the average of the forward and backward stencils used at the boundary point for the prefactored method. At the second interior point, however, an explicit stencil is used for the standard compact scheme, whereas the prefactored scheme is already using the interior stencil.

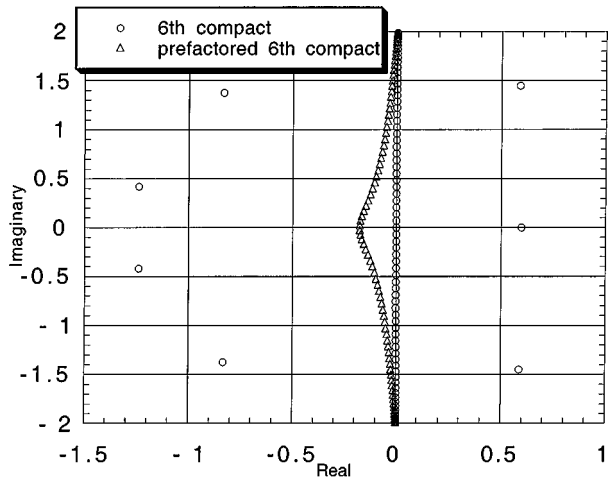

FIG. 3. Spectral eigenvalue analysis of standard and prefactored compact schemes.

Figure 3 shows the results of this analysis for both schemes, illustrating that the prefactored scheme is stable with this boundary stencil specification, whereas the standard scheme is unstable. This suggests that the reduction in the number of boundary stencils makes the prefactored scheme more stable.

It should be noted here that the stencils given are not the only possible boundary stencils for these schemes, and that stable boundary stencils exist for the standard sixth-order compact scheme. In Ref. [16], Carpenter *et al.* proposed stable boundary stencils for high-order compact schemes, at the cost of increased complexity near the boundary points. Another approach was taken by Lele [3], who proposed fourth-order stencils which were conservative and stable. Since the boundary stencils described above were shown to be linearly stable for the prefactored scheme and have been tested extensively on realistic problems (e.g., Refs. [25, 26]), they were used throughout this work.

6.3. *Interior Boundaries*

In realistic computations, computational boundaries exist where the flow data are known on both sides of the boundary (for example, periodic, symmetry, and block boundaries). Thus, it is appropriate to use the interior differencing scheme at the boundary point.

There are two ways to accomplish this. This first method is to use the one-sided boundary stencils of Eqs. (30)–(33) to provide an initial guess to start the sweep; when an updated value for the boundary derivative becomes available, Eq. (27) is used to update the interior derivatives near the boundary. For a multiblock calculation, however, this can be computationally inefficient.

The second strategy is to derive a central explicit boundary stencil which mimics the performance of the compact interior stencil over the resolved range of wavenumbers. The computational sweep is then started using this central stencil; since the error from the stencil is low, no derivative update is required.

To accomplish this, an 11-point explicit stencil was derived. This stencil matches the Taylor series of the interior stencil to the ninth order, with the last coefficient used to more closely match the boundary stencil performance with that of the interior stencil.

The interior boundary stencils are given by

$$D_i^F = \sum_{j=-5}^{5} b_j f_{i+j}$$
$$D_i^B = \sum_{j=-5}^{5} -b_{-j} f_{i+j}, \tag{34}$$

where

$$\begin{aligned} b_{-5} &= -0.0005487 \\ b_{-4} &= 0.0057215 \\ b_{-3} &= -0.0274597 \\ b_{-2} &= 0.0805155 \\ b_{-1} &= -0.3281347 \\ b_0 &= -0.7500340 \\ b_1 &= 1.3347370 \\ b_2 &= -0.3922902 \\ b_3 &= 0.0905768 \\ b_4 &= -0.0141906 \\ b_5 &= 0.0011070. \end{aligned} \tag{35}$$

Since these are central stencils, the same stencil is used at the start and the end of each sweep.

Figure 4 shows the result of a spectral eigenvalue analysis performed using Eq. (34). Two results are shown: the first has no interior boundary stencils, while the second has interior

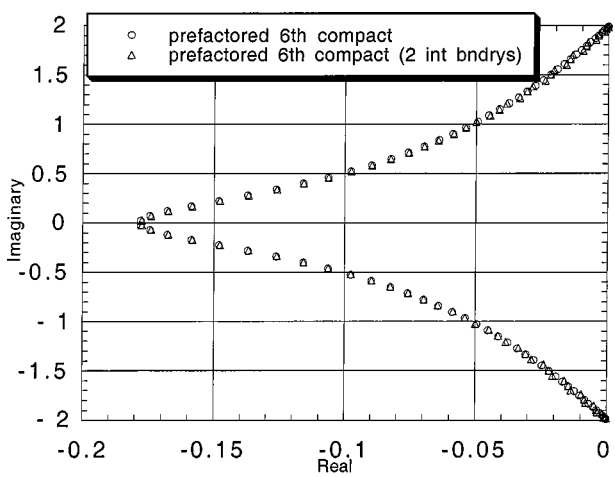

FIG. 4. Spectral eigenvalue analysis of prefactored compact scheme using explicit interior boundary stencils.

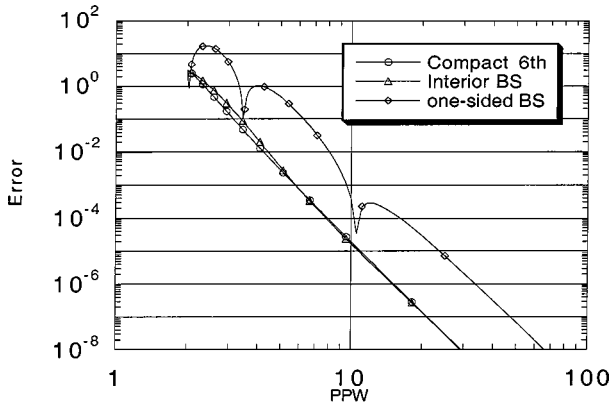

FIG. 5. Wavenumber performance of explicit boundary stencils.

boundary stencils at grid points 30 and 55. It is seen that the performance of the scheme is changed very little by using these interior boundaries.

Figure 5 shows the performance of the boundary stencils given above. The interior boundary stencil of Eqs. (34) and (35) performs very well, while the one-sided difference of Eqs. (30)–(33) returns more error. However, it is unlikely that a one-sided difference of such high order could be made to have better performance. The stencils described above will be used for the benchmark problem tests.

7. TIME-MARCHING SCHEME

The time-marching scheme used is the 4–6 Low Dispersion and Dissipation Runge–Kutta (LDDRK) optimized scheme of Hu *et al.* [19]. The 4–6 notation signifies a two-step marching cycle where four stages are used for the first time step and six stages for the second time step in the cycle. This scheme is fourth-order accurate in time for linear problems and second-order accurate for nonlinear problems.

The storage requirements for the 4–6 method are three levels of data storage, as opposed to four levels for the classical fourth-order Runge–Kutta scheme. By storing an addtional level of data or adding an additional stage in the first step, this method can be extended to fourth-order nonlinear accuracy; however, the scheme used in this work is only second-order accurate for nonlinear problems.

The advantage of the LDDRK 4–6 method is that the optimization used reduces the error from one to three orders of magnitude for a given time step compared to the classical fourth-order Runge–Kutta scheme. Since the 4–6 method is effectively using five stages per time step as opposed to four stages per time step for the classical scheme, there is a 25% increase in the amount of work per step. However, to reduce the error by just one order of magnitude, a fourth-order scheme must reduce the time step by a factor of 0.56, requiring 1.78 times more work. Thus, the optimized scheme reduces the actual amount of work required for a given level of error.

This method has been previously tested and found to be very accurate and stable for unsteady problems [10]. Using this time-stepping method, the sixth-order compact scheme is stable to a CFL limit of 1.266. It should be noted that the classical scheme has a slightly larger range of stability; however, the accuracy at large time steps is not acceptable for long-term time-accurate calculations.

8. PREFACTORED COMPACT DISSIPATION

When solving nonlinear equations, artificial dissipation must be added to damp spurious high-frequency waves generated in the solution. From Eq. (17), it is clear that compact dissipation can be defined as

$$D^{\text{diss}} = \frac{A}{2}(D^F - D^B), \tag{36}$$

where A is a user input scaling factor.

By defining the forward and backward stencils such that the coefficient of the second derivative error term in Eq. (17) is zero, a fourth-order compact difference remains. Using Eq. (9), we get

$$\begin{aligned} a &= \frac{1}{3} \\ b &= \frac{1}{6} \\ c &= 0. \end{aligned} \tag{37}$$

This scheme is derived in Ref. [12] and called a 4–4 scheme. In more recent work, several high-accuracy compact filters have been prefactored and tested [20].

9. BENCHMARK TEST PROBLEMS AND RESULTS

Three test problems were chosen to investigate the numerical performance of the new sixth-order compact scheme. These problems are from the First [21] and Second [22] CAA Workshops.

9.1. *1-D Linear Wave Propagation*

This benchmark problem asks for the solution at time =400 of the 1-D linear convection equation

$$\frac{dU}{dt} + \frac{dU}{dx} = 0, \tag{38}$$

where

$$\begin{aligned} U(x,0) &= \frac{1}{2}e^{-(\ln(2))(x/3)^2} \\ \Delta x &= 1.0 \\ -20 &\le x \le 450. \end{aligned} \tag{39}$$

Boundary condition specification is straightforward in this problem. At the inflow boundary ($x = -20$), U is set equal to zero. At the outflow boundary ($x = 450$), U is calculated by the code using the one-sided explicit boundary stencils.

Figure 6 shows the result for the sixth-order compact scheme at time =400, compared to the exact solution and the same scheme using the explicit 7-point DRP method. The time step used is $\Delta t = 1.25$. The compact solution compares very well.

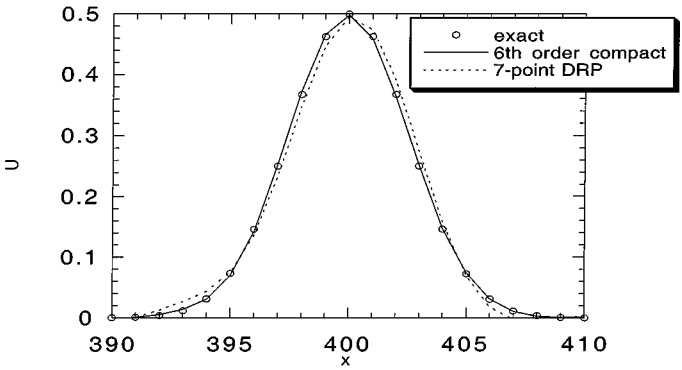

FIG. 6. Solution of linear wave problem at time = 400.

Figure 7 shows the boundary stencil performance as the wave exits the domain. The waveform remains consistent as it exists, without spurious waves being generated.

9.2. *Nonlinear Shock Tube Problem*

The second 1-D problem solves the Category 2 shock tube problem from the First CAA Workshop [21]. The equations are the nonlinear Euler equations, solved in conservative form,

$$\frac{d}{dt}\begin{Bmatrix}\rho\\ \rho u\\ E\end{Bmatrix}+\frac{d}{dx}\begin{Bmatrix}\rho u\\ \rho u^2+p\\ u(E+p)\end{Bmatrix}=0, \tag{40}$$

where

$$p=(\gamma-1)\left(E-\frac{1}{2}\rho u^2\right). \tag{41}$$

The equations are solved on the domain $-235 < x < 235$, with $\Delta x = 1.0$.

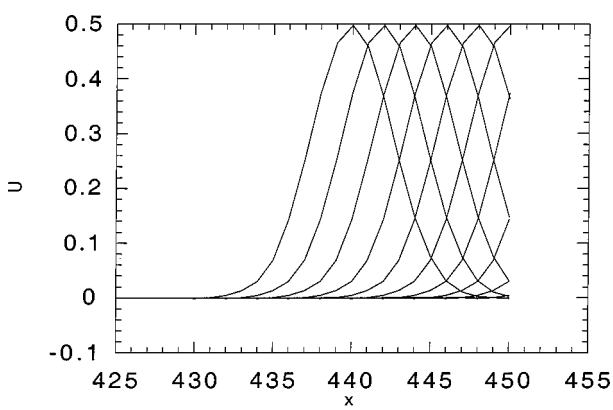

FIG. 7. Boundary stencil performance for linear wave problem.

The initial conditions are

$$
\begin{aligned}
&u(x,0) = 0. \\
&p(x,0) = \begin{cases} 4.4 & x < -2 \\ 2.7 + 1.7\cos\left(\frac{(x+m2)\pi}{4}\right) & -2 \le x \le 2 \\ 1.0 & x > 2. \end{cases} \\
&\rho(x,0) = (\gamma p)^{1/\gamma}.
\end{aligned} \tag{42}
$$

The boundary conditions used are Thompson's 1-D characteristic formulation [13, 14]. For 1-D, three characteristics are defined,

$$
\begin{aligned}
c_1 &= \frac{dp}{dt} - \bar{\rho}\bar{c}\frac{du}{dt} \\
c_2 &= \bar{c}^2\frac{d\rho}{dt} - \frac{dp}{dt} \\
c_3 &= \frac{dp}{dt} + \bar{\rho}\bar{c}\frac{du}{dt},
\end{aligned} \tag{43}
$$

where the overbar terms are set to the initial values at each boundary. For the inflow boundary ($x = -235$), c_1 and c_2 are incoming and are set to zero. For the outflow boundary ($x = 235$), c_3 is incoming and is set to zero.

In this calculation, the compact 4th-order dissipation described in Section 8 is used, with a coefficient of $A = 0.25$. The value of A was chosen based on numerical tests which showed that this value gave the minimum damping that allowed stability for this problem. While the addition of 4th-order dissipation reduces the order of the scheme to 3rd order, the discontinuities in the flow will only allow the scheme to obtain a 1st-order accurate solution. In more recent nonlinear flow calculations, an explicit 10th-order filter was used in conjunction with a 4th-order nonlinear time marching scheme [25, 26].

Figure 8 shows results for the density profile at time $=60$, compared with the exact solution. In this calculation, a time step of CFL $= 0.5$ was used. The expansion fan, contact patch, and shock are all captured, with correct propagation speeds. The compact dissipation controls the oscillations near the shock, but a better dissipation model would give cleaner results.

It should be noted, however, that the exact solution shown is for a discontinuous initial condition at $x = 0$; thus, it does not compare exactly with the initial conditions given in Eq. (42). The difference in initial conditions causes a slightly different solution near the contact patch and expansion fan, which can be seen in Fig. 8.

Figure 9 shows the results obtained at time $=300$. By this point, both the shock wave and the expansion fan have hit the boundary, while the contact patch is still in the computational domain. Due to the linearized nature of the boundary condition, a small shock is reflected in from the outflow boundary, and is seen traveling to the left. However, the sixth-order compact scheme is stable throughout this calculation.

9.3. *2-D Acoustic Scattering Problem*

This test problem is from the Second CAA Workshop [22]. In this problem, a 2-D cylinder of radius $R = 0.5$ is located at the origin. At time $= 0$, an initial pressure transient

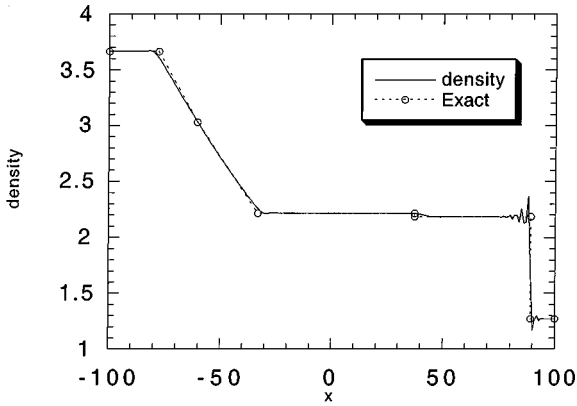

FIG. 8. Solution of shock tube problem at time = 60.

is specified:

$$p(x, y, 0) = e^{-\ln(2)([(x-4)^2+y^2]/0.04)}. \tag{44}$$

The problem asks for the unsteady pressure data from time =6–10 at $R = 5.0$ for three azimuthal stations: $\theta = 90^\circ$, 135°, and 180°.

The equations to be solved are the linearized Euler equations in polar coordinates:

$$\frac{d}{dt}\begin{Bmatrix} v_r \\ v_\theta \\ p \end{Bmatrix} + \frac{d}{dr}\begin{Bmatrix} p \\ 0 \\ v_r \end{Bmatrix} + \frac{1}{r}\frac{d}{d\theta}\begin{Bmatrix} 0 \\ p \\ v_\theta \end{Bmatrix} = \frac{1}{r}\begin{Bmatrix} 0 \\ 0 \\ v_r \end{Bmatrix}. \tag{45}$$

The computational domain extends radially from $R = 0.5$ to $R = 10.5$. Azimuthally, the domain covers the half-plane $\theta = 0$ to $\theta = \pi$. Three boundary conditions are used: a wall condition on the cylinder, an acoustic radiation condition in the far field, and a symmetry condition at the azimuthal boundaries.

The wall condition is based on the wall condition of Tam and Dong [15]. This requires that the change of the normal velocity at the wall be zero:

$$\frac{dv_r}{dt} = -\frac{dp}{dr} = 0. \tag{46}$$

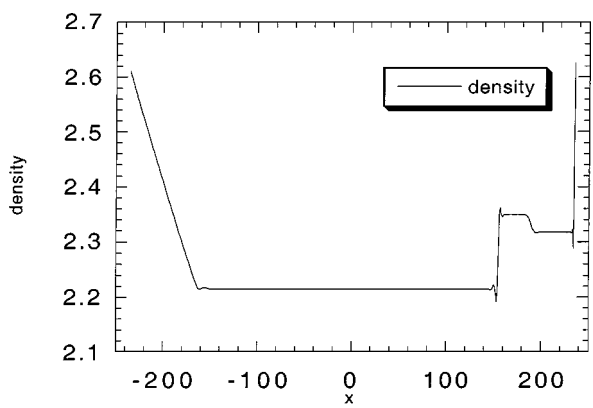

FIG. 9. Boundary stencil performance for shock tube problem (time = 300).

This condition is imposed by calculating the radial derivative of pressure at the wall on the forward sweep and setting the radial pressure derivative at the wall for the backward sweep, using

$$D^B_{\text{wall}}(p) = -D^F_{\text{wall}}(p). \tag{47}$$

The other radial conditions are computed normally, using one-sided boundary stencils. The acoustic radiation condition of Bayliss and Turkel [23, 24] is given as

$$\frac{d}{dt}\begin{Bmatrix} v_r \\ v_\theta \\ p \end{Bmatrix} + \frac{d}{dr}\begin{Bmatrix} v_r \\ 0 \\ p \end{Bmatrix} + \frac{1}{2r}\frac{d}{d\theta}\begin{Bmatrix} v_r \\ 0 \\ p \end{Bmatrix} = 0. \tag{48}$$

The radial derivatives at the outer boundary are computed using one-sided boundary stencils.

The symmetry boundary condition is set using explicit interior stencils. At the symmetry boundary,

$$\begin{aligned} \frac{dv_r}{d\theta} &= 0 \\ v_\theta &= 0 \\ \frac{dp}{d\theta} &= 0. \end{aligned} \tag{49}$$

This allows the values of the flow quantities to be reflected across the symmetry boundary; thus, the explicit interior stencil can be used to start and end the sweeps.

FIG. 10. Snapshot of pressure at time = 7.5 for 2-D linear wave.

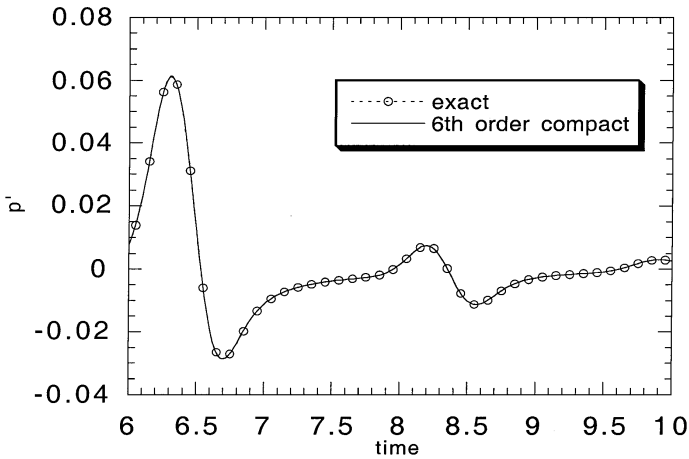

FIG. 11. Pressure history at point A for 2-D linear benchmark problem.

For this calculation, a uniformly spaced grid of 201 radial points and 151 azimuthal points was used, with a time step of CFL = 1.0. Figure 10 shows a snapshot of the perturbation pressure at time = 7.5. In this figure, the acoustic pulse has reflected from the cylinder and reached the outer boundary.

Figure 11 and 12 compare the solution given by the sixth-order compact scheme with the exact solution for $\theta = 90^\circ$ and 180°. The results are extremely good, even with this relatively coarse mesh.

Figure 13 shows the effect of grid resolution on the solution at $\theta = 90^\circ$. In this series of tests, the radial resolution is set at either 101 or 201 points, and the azimuthal resolution is set at either 101 or 151 points. In the solution at $\theta = 90^\circ$, two main transients are shown. The first, and larger, travels directly from the initial pulse, and is mainly dependent on the azimuthal grid resolution. The smaller secondary pulse is the reflection from the cylinder, and is mainly dependent on the radial grid resolution. Figure 13 shows that the accuracy of the scheme is still evident even with marginal resolution.

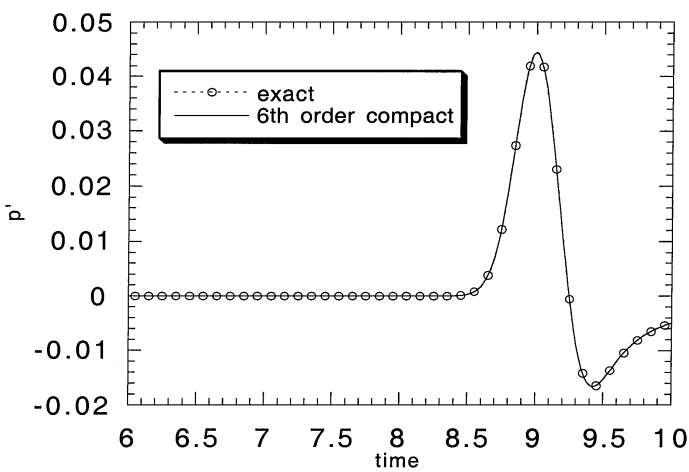

FIG. 12. Pressure history at point B for 2-D linear benchmark problem.

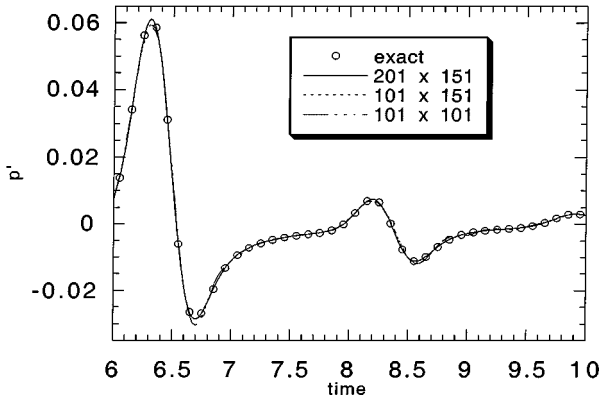

FIG. 13. Grid resolution effect on 2-D linear benchmark problem solution.

10. CONCLUSIONS

A new series of prefactored compact differencing schemes which use very small stencils are presented. The factorization reduces the tridiagonal matrix of the original sixth-order compact scheme into independent upper and lower bidiagonal matrices, which are solved in parallel. The stencil size is also reduced from five points to three; due to the smaller stencil size, only one boundary stencil is needed instead of two. The prefactorization method makes boundary condition implementation much more straightforward than the standard schemes. Several boundary stencils are described, and the stability and accuracy of the scheme is shown using benchmark problems of the First and Second CAA Workshops. This method has since been applied to nonlinear unsteady flows with complex geometries [25, 26] and has performed very well.

ACKNOWLEDGMENTS

This work was conducted under Grant NCC3-531 from the NASA Glenn Research Center while the author was in residence at the Institute for Computational Mechanics in Propulsion at the Ohio Aerospace Institute. Dr. L. A. Povinelli was the Technical Monitor.

REFERENCES

1. H. O. Kreiss, S. A. Orszag, and M. Israeli, *Annu. Rev. Fluid Mech.* **6**, 281 (1974).
2. D. Gottlieb and E. Turkel, Dissipative two–four method for time dependent problems, *Math. Comput.* **30**, 703 (1976).
3. S. K. Lele, Compact finite difference schemes with spectral-like resolution, *J. Comput. Phys.* **103**, 16 (1992).
4. C. K. W. Tam and J. C. Webb, Dispersion relation preserving finite difference schemes for computational acoustics, *J. Comput. Phys.* **107**, 262 (1993).
5. D. W. Zingg, H. Lomax, and H. M. Jurgens, An optimized finite-difference scheme for wave propagation problems, *SIAM J. Sci. Comput.* **17**, 328 (1996).
6. Z. Haras and S. Ta'asan, Finite-difference schemes for long-time integration, *J. Comput. Phys.* **114**, 265 (1994).
7. S.-T. Yu, K.-C. Hsieh, and Y.-L. P. Tsai, Simulating waves in flows by Runge–Kutta and compact difference schemes, *AIAA Journal* **33**, 421 (1995).

8. R. K. Agarwal and K. S. Huh, A dispersion-relation preserving fourth-order compact time-domain frequency-domain finite-volume method for computational acoustics, *AIAA 33rd Aerospace Sciences Meeting and Exhibit, Reno, NV, 1996, AIAA Paper 96-0277*.
9. J. W. Kim and D. J. Lee, Optimized compact finite difference schemes with maximum resolution, *AIAA J.* **34**, 887 (1996).
10. R. Hixon, On increasing the accuracy of MacCormack schemes for aeroacoustic applications, *AIAA Paper 97-1586, 3rd AIAA/CEAS Aeroacoustics Conference (Atlanta, GA, 1997* (unpublished)*)*.
11. R. Hixon, Evaluation of a high-accuracy MacCormack-type scheme using benchmark problems, *J. Comput. Acoust.* **6**, 291 (1998).
12. R. Hixon and E. Turkel, High-accuracy compact MacCormack-type schemes for computational aeroacoustics, *J. Comput. Phys.* **158**, 51 (2000).
13. K. W. Thompson, Time-dependent boundary conditions for hyperbolic systems, *J. Comput. Phys.* **68**, 1 (1987).
14. K. W. Thompson, Time-dependent boundary conditions for hyperbolic systems, II, *J. Comput. Phys.* **89**, 439 (1990).
15. C. K. W. Tam and Z. Dong, Wall boundary conditions for high-order finite difference schemes in computational aeroacoustics, *Theor. Comput. Fluid Dynam.* **6**, 303 (1994).
16. M. H. Carpenter, D. Gottlieb, and S. Abarbanel, Stable and accurate boundary treatments for compact, high-order finite-difference schemes, *Appl. Numer. Math.* **12**, 55 (1993).
17. M. H. Carpenter, D. Gottlieb, and S. Abarbanel, Time-stable boundary conditions for finite-difference schemes solving hyperbolic systems: Methodology and application to high-order compact schemes, *J. Comput. Phys.* **111**, 220 (1994).
18. J. W. Kim and D. J. Lee, Implementation of boundary conditions for the optimized high-order compact schemes, *AIAA Paper 96-1665, presented at the AIAA/CEAS 2nd Aeroacoustics Conference, State College, PA*, 1996.
19. F. Q. Hu, M. Y. Hussaini, and J. Manthey, Low-dissipation and -dispersion Runge–Kutta schemes for computational acoustics, *J. Comput. Phys.* **124**, 177 (1996).
20. R. Hixon, Prefactored compact filters for computational aeroacoustics, *AIAA Paper 99-0358, presented at the AIAA 36th Aerospace Sciences Meeting and Exhibit, Reno, NV*, 1999.
21. C. K. W. Tam, Benchmark problems, in *ICASE/LaRC Workshop on Benchmark Problems in Computational Aeroacoustics* (1995), NASA CP-3300, p. 1.
22. C. K. W. Tam and J. C. Hardin, (Eds.), *Second Computational Aeroacoustics Workshop on Benchmark Problems* (1997), NASA CP-3352.
23. A. Bayliss and E. Turkel, Radiation boundary conditions for wave-like equations, *Commun. Pure Appl. Math.* **33**, 707 (1980).
24. A. Bayliss and E. Turkel, Far field boundary conditions for compressible flows, *J. Comput. Phys.* **48**, 182 (1982).
25. R. Hixon, S.-H. Shih, R. R. Mankbadi, and J. R. Scott, Time-domain solution of the airfoil gust problem using a high-order compact scheme, presented at the *34th AIAA/ASME/SAE/ASEE Joint Propulsion Conference and Exhibit (1998), AIAA Paper 98-3241*.
26. R. Hixon, S.-H. Shih, and R. R. Mankbadi, Evaluation of boundary conditions for the gust–cascade problem, *J. Propulsion Power* **16**, 72 (2000).